The Astrophysical Journal, 878:86 (9pp), 2019 June 20 https://doi.org/10.3847/1538-4357/ab204b

A Physical Basis for the *H*-band Blue-edge Velocity and Light-curve Shape Correlation in Context of Type Ia Supernova Explosion Physics

C. Ashall[1], P. Hoeflich[1], E. Y. Hsiao[1], M. M. Phillips[1,2], M. Stritzinger[3], E. Baron[3,4,5], A. L. Piro[6], C. Burns[6], C. Contreras[2], S. Davis[1], L. Galbany[7], S. Holmbo[3], R. P. Kirshner[8,9], K. Krisciunas[10], G. H. Marion[11], N. Morrell[2], D. J. Sand[12], M. Shahbandeh[1], N. B. Suntzeff[10], and F. Taddia[3]

[1] Department of Physics, Florida State University, Tallahassee, FL 32306, USA; Chris.Ashall@gmail.com
[2] Carnegie Observatories, Las Campanas Observatory, 601 Casilla, La Serena, Chile
[3] Department of Physics and Astronomy, Aarhus University, Ny Munkegade 120, DK-8000 Aarhus C, Denmark
[4] Homer L. Dodge Department of Physics and Astronomy, University of Oklahoma, 440 W. Brooks, Rm. 100, Norman, OK 73019-2061, USA
[5] Hamburger Sternwarte, Gojenbergsweg 112, D-21029 Hamburg, Germany
[6] Observatories of the Carnegie Institution for Science, 813 Santa Barbara Street, Pasadena, CA 91101, USA
[7] PITT PACC, Department of Physics and Astronomy, University of Pittsburgh, Pittsburgh, PA 15260, USA
[8] Gordon and Betty Moore Foundation, 1661 Page Mill Road, Palo Alto, CA 94304, USA
[9] Harvard-Smithsonian Center for Astrophysics, 60 Garden Street, Cambridge, MA 02138, USA
[10] George P. and Cynthia Woods Mitchell Institute for Fundamental Physics & Astronomy, Texas A&M University, Department of Physics, 4242 TAMU, College Station, TX 77843, USA
[11] University of Texas at Austin, 1 University Station C1400, Austin, TX, 78712-0259, USA
[12] Department of Astronomy/Steward Observatory, 933 North Cherry Avenue, Rm. N204, Tucson, AZ 85721-0065, USA
Received 2019 February 18; revised 2019 May 7; accepted 2019 May 7; published 2019 June 18

Abstract

Our recent work demonstrates a correlation between the high-velocity blue edge, $v_{\rm edge}$, of the iron-peak Fe/Co/Ni *H*-band emission feature and the optical light-curve (LC) shape of normal, transitional and subluminous SNe Ia. We explain this correlation in terms of SN Ia physics. $v_{\rm edge}$ corresponds to the sharp transition between the complete and incomplete silicon burning regions in the ejecta. It measures the point in velocity space where the outer ^{56}Ni mass fraction, $X_{\rm Ni}$, falls to the order of 0.03–0.10. For a given ^{56}Ni mass, $M(^{56}{\rm Ni})$, $v_{\rm edge}$ is sensitive to the specific kinetic energy $E_{\rm kin}(M(^{56}{\rm Ni})/M_{\rm WD})$ of the corresponding region. Combining $v_{\rm edge}$ with LC parameters (i.e., s_{BV}, $\Delta m_{15,s}$ in *B* and *V*) allows us to distinguish between explosion scenarios. The correlation between $v_{\rm edge}$ and light-curve shape is consistent with explosion models near the Chandrasekhar limit. However, the available sub-$M_{\rm Ch}$ WD explosion model based on SN 1999by exhibits velocities that are too large to explain the observations. Finally, the subluminous SN 2015bo exhibits signatures of a dynamical merger of two WDs demonstrating diversity among explosion scenarios at the faint end of the SNe Ia population.

Key words: supernovae: general

1. Introduction

Significant evidence supports the idea that SNe Ia result from the thermonuclear explosions of at least one carbon–oxygen (C-O) white dwarf (WD) in a binary system. There are two main progenitor channels that have been hypothesized to produce these cosmic explosions. These are the single degenerate scenario (SDS), and the double-degenerate scenario (DDS). In the SDS a WD accretes material from a nondegenerate companion star such as a H/He or red giant star (Whelan & Iben 1973; Livne 1990; Woosley & Weaver 1994; Nomoto et al. 1997), whereas in the DDS the system consists of two WDs.

Within each progenitor scenario, multiple explosion mechanisms have been explored. One method for exploding an SN Ia is with heat released during the dynamical merging of two WDs (e.g., Dan et al. 2014, 2015).

Alternatively, when a WD approaches the Chandrasekhar mass ($M_{\rm Ch}$) the explosion can be triggered by compressional heating in the center. This possibility may occur in both the SDS (Hoeflich & Khokhlov 1996; Nomoto et al. 1997), as well as in the DDS scenario where a tidally disrupted WD accretes onto the primary WD on secular timescales, which are much longer than the hydro-dynamical timescales (Piersanti et al. 2003). In a $M_{\rm Ch}$ explosion the nuclear burning flame front begins as a subsonic deflagration wave and then at a particular transition density, $\rho_{\rm tr}$, it evolves into a supersonic detonation wave. This is known as a delayed detonation (DDT) model and has been shown to provide a good match to spectra and light curves (LCs) of SNe Ia (Khokhlov 1991; Yamaoka et al. 1992; Hoeflich & Khokhlov 1996; Gamezo et al. 2005; Blondin et al. 2011, 2015; Poludnenko et al. 2011; Hoeflich et al. 2017; Ashall et al. 2018). For DDT explosions the luminosity of the SN is correlated with the amount of burning during the deflagration phase (Gamezo et al. 2005; Röpke et al. 2007; Jordan et al. 2008), which in spherical models is parameterized by $\rho_{\rm tr}$, where less luminous objects have a lower $\rho_{\rm tr}$ value (Hoeflich & Khokhlov 1996; Hoeflich et al. 2017). Effectively, a low $\rho_{\rm tr}$ produces more intermediate mass elements (IME) at the expense of ^{56}Ni, and for less luminous objects the remaining ^{56}Ni is located at lower velocities.

Another possibility is the explosion of a sub-$M_{\rm Ch}$ WD in the so-called edge-lit, or double-detonation scenario. Here, He accreted from a companion star onto the surface of the WD detonates, which drives a shock wave inward igniting the center of the WD, while the outer layer is consumed by the initial detonation (Woosley & Weaver 1994; Livne & Arnett 1995; Hoeflich & Khokhlov 1996; Nugent et al. 1997; Fink et al. 2007; Pakmor et al. 2012; Shen & Moore 2014). These models have recently made a revival as it has been shown that by mixing the outer He layer with a small amount of

C alters the burning network from slow triple-α to the fast $^{12}C(\alpha, \gamma)^{16}O$ channel (Shen & Moore 2014). This reduces the mass of the He shell required to form a sustained nuclear detonation by an order of magnitude compared to previous work (e.g., Woosley & Weaver 1994; Livne & Arnett 1995). The resulting density structures are close to spherical with small polarization (Bulla et al. 2016a), and to first order, the outer layers hardly affect the LCs beyond ≈1 week after the explosion (Polin et al. 2018). However, it is not clear whether the reduced He mass can trigger a detonation in the C/O layers of the WD. In sub-M_{Ch} models the luminosity of the SN is correlated with the ejecta mass of the explosion, where less luminous objects have a smaller WD mass (M_{WD}); (Sim et al. 2010; Blondin et al. 2017).

The luminosity of an SN Ia is dependent on the amount of ^{56}Ni synthesized in the explosion. More luminous SNe produce larger amounts of ^{56}Ni (e.g., Arnett 1982; Stritzinger et al. 2006; Mazzali et al. 2007; Childress et al. 2015). Furthermore, events that are more luminous also have broader LCs, which is the underlying basis for the luminosity–width relation (LWR) (Phillips 1993; Phillips et al. 1999). The LWR can be understood in terms of opacities, where brighter objects have more ^{56}Ni, produce more heating, are dominated by doubly ionized species, and therefore have slowly evolving LCs. Whereas, the faintest SNe Ia have less ^{56}Ni, less heating, are dominated by singly ionized species, and have faster LCs (Nugent et al. 1997; Umeda et al. 1999; Kasen et al. 2009; Hoeflich et al. 2017).

At the faint end of the LWR, there are subluminous SNe Ia (1991bg-like; Filippenko et al. 1992; Leibundgut et al. 1993; Turatto et al. 1996). The literature contains a number of different scenarios accounting for the origins of subluminous SNe Ia. These extend from the dynamical merger of two WDs[13] (García-Berro & Lorén-Aguilar 2017), to sub-M_{Ch} explosions (Scalzo et al. 2014; Blondin et al. 2017, 2018), and to M_{Ch} DDT explosions (Hoeflich et al. 2002, 2017). A key to understanding SNe Ia is to address the ongoing question of whether normal, transitional[14] and subluminous SNe Ia are separate groups, form a continuum, or are a mixture of diverse scenarios. This work aims to address this question.

The ongoing discussion about explosion scenarios in SNe Ia physics may, at least in part, be attributed to different assumptions in the modeling process. These assumptions include LTE population levels (e.g., Goldstein & Kasen 2018), a small atomic network of isotopes (e.g., Polin et al. 2018), and that M_{Ch} explosions do not have a central core of electron capture elements. On the other hand, we know non-LTE effects are important, and, even full non-LTE simulations result in different conclusions on the nature of subluminous SNe Ia, see Hoeflich et al. (2002, 2017) and Blondin et al. (2017, 2018).

NIR spectroscopy offers a promising way to investigate the physics of SNe Ia. In the *H* band, between maximum light and +10 days, an emission component is formed by blends of a large number of emission lines above the photosphere (Wheeler et al. 1998; Hoeflich et al. 2002; Hsiao 2009; Hsiao et al. 2013). This *H*-band feature consists of a multiplet of many allowed Fe II/Co II/Ni II lines formed within the ^{56}Ni-rich layers and is thus correlated with the luminosity of the SN (Hsiao et al. 2013; Ashall et al. 2019).

One of the main objectives of the Carnegie Supernova Project II (CSP-II; Phillips et al. 2019) was to obtain a large sample of NIR spectra of SNe Ia (Hsiao et al. 2019). Using this data, Ashall et al. (2019) found a correlation between the outer blue-edge velocity, v_{edge}, of the *H*-band break region and the optical light-curve shape for normal, transitional, and sub-luminous SNE Ia.[15] Here, we explain this correlation in terms of SNe Ia physics and models. We compare the data to both spherical sub-M_{Ch} and M_{Ch} explosion models with non-LTE LCs and spectra published in the literature. We use 1D calculations as they artificially suppress mixing and produce a chemically layered structure. This is in line with both observations (Fesen et al. 2007; Maeda et al. 2010; Dhawan et al. 2018; Diamond et al. 2018) and inferred abundance stratification results (e.g., Stehle et al. 2005; Tanaka et al. 2011; Ashall et al. 2016b). This suppressed mixing may be due to high magnetic fields (Hristov et al. 2018).

In this work, we show how v_{edge} varies among different explosion models, even for SNe with similar ^{56}Ni masses. Therefore, v_{edge} provides new information beyond the total amount of ^{56}Ni synthesized in the explosion, which has been classically used to analyze SNe Ia (Stritzinger et al. 2006; Childress et al. 2015; Dhawan et al. 2017; Scalzo et al. 2019). A second goal of this paper is to put v_{edge} into context with the classical characterization using SNe Ia LC shape and absolute magnitude, and to show an example of how this combined information can be used to distinguish between explosion models.

2. Measurements of Spectra and LC Parameters

In this work, the *H*-band break is represented by the Doppler shift, v_{edge}, of the bluest component of the *H*-band multiplet at 1.57 μm (Figure 1). In an SN Ia explosion, the photosphere recedes through the IME layers before it reaches the ^{56}Ni region. Once this ^{56}Ni-rich region is exposed, the Fe/Co/Ni emission in the *H*-band begins to emerge. Ashall et al. (2019) found that at about +10 days relative to *B*-band maximum was a good time to measure v_{edge}, because during this phase the spectra are dominated by single ionized iron-group elements, and by then the feature has emerged in all SNe Ia. However, note that at earlier times, v_{edge} may be affected by lines of IME. Whereas, significantly beyond +10 days the emission from forbidden lines starts to dominate. In fact, the ideal time to measure v_{edge} may be right after the *H*-band feature can be clearly distinguished from other blends. However, this would require daily observations, which are not currently available.

We measure v_{edge} by the method outlined in Ashall et al. (2019) in both the observed and theoretical spectra. Briefly, v_{edge} is measured by fitting a Gaussian profile to the minimum of the blue edge of the *H*-band break. The fit is produced over a fixed wavelength range and iterated to find convergence. The model spectra are based on detailed non-LTE radiation transport explosions for normal, transitional and subluminous SNe Ia (Hoeflich et al. 2002, 2017; Blondin et al. 2018). For all models close to M_{Ch}, v_{edge} corresponds to the region where the ^{56}Ni mass fraction, X_{Ni}, is approximately 0.02–0.03. For the subluminous sub-M_{Ch} model with low mass ($M_{WD} = 0.9M_{\odot}$) (Blondin et al. 2018) the corresponding abundance is slightly

[13] For normal SNe Ia this is currently out of favor as it is inconsistent with low polarization observations (Patat et al. 2012; Bulla et al. 2016b).

[14] Transitional SNe Ia are thought to be the link between the normal and subluminous populations (e.g., see Hsiao et al. 2015; Ashall et al. 2016a, 2016b; Gall et al. 2018).

[15] We note that this work does not include analyses of other SNe Ia sub-type objects such as SN 1991T or SNe Iax.

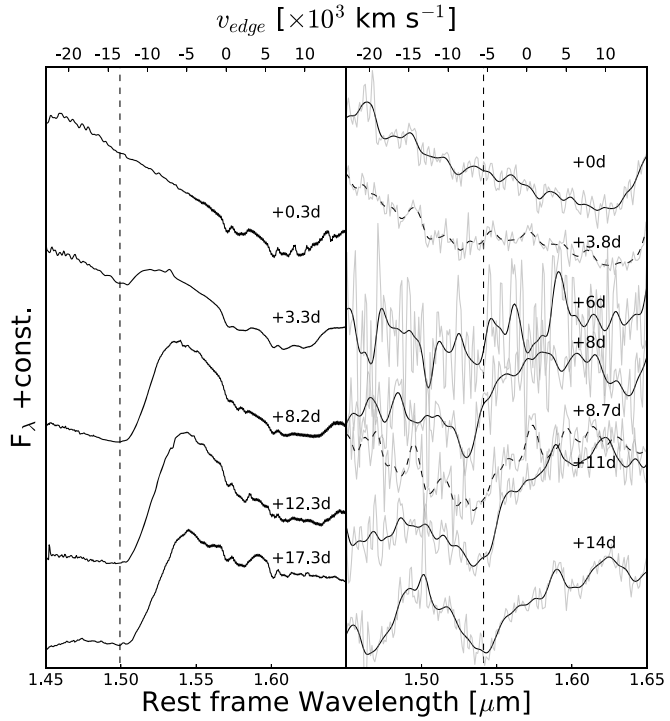

Figure 1. Comparison of the *H*-band region of a normal SN Ia (left) and a subluminous SN Ia (right). Left: a time series of spectra of SN 2011fe (Hsiao et al. 2013). The vertical dashed line is the blue edge of the +12.3 day spectra ($-13{,}500$ km s^{-1}). Right: a combined time series of spectra for SN 1999by (solid; Hoeflich et al. 2002) and ASASSN-15ga (dashed). The spectra were Gaussian smoothed (2σ), and the underlying unsmoothed spectra are plotted in light gray. The vertical dashed line is the blue edge of the +11 day spectra at -5500 km s^{-1}. Times are given relative to rest-frame *B*-band maximum.

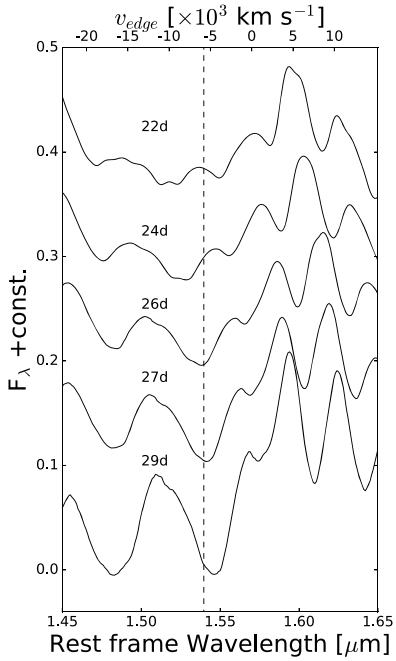

Figure 2. Time series of model spectra of a subluminous SN Ia from Hoeflich et al. (2002). It can be seen that at the earlier epochs the value of $v_{\rm edge}$ could be affected by blends from IMEs. Times are given relative to the explosion. The rise time of the SN is $\sim$14.5 $\pm$ 0.5 days. The vertical dashed line is a value of $v_{\rm edge}$ (-5800 km s^{-1}) at 26 days past explosion, or +11.5 $\pm$ 0.5 days from maximum.

higher ($X_{\rm Ni}$ is $\approx$0.10).[16] This is because the lower mass produces a smaller optical depth. For all models, regardless of $M_{\rm WD}$, the value of $X_{\rm Ni}$ is small. Therefore, we use the *H*-band break as an indicator for the outer edge of the ^{56}Ni region. For a discussion of the uncertainties in the fluxes see the references for each of the models.

In Figure 1, we present observations of the spectral evolution for a normal-bright and a subluminous SN Ia. For bright SNe Ia, the iron-peak feature emerges at about +3 days past maximum light when the overall NIR continuum is dominated by Thomson scattering and, thus, will have very little line blending beyond the blue edge. For the subluminous example, blends of other transitions are obvious in both the observations and the theoretical model, because they have a lower ionization state and less Thomson scattering (Figure 2). These blends can be seen until about +10 days, and can be attributed to lines of singly ionized iron-group elements, Ca II and Ca I (1.46, 1.51 μm) and neutral IME elements, namely Si I (1.52 μm), S I (1.46, 1.54 and 1.52, 1.57 μm) (Hoeflich et al. 2002). Therefore, for subluminous SNe Ia, spectra should be inspected to make sure there are no blends of IMEs.[17] However, even for the least luminous objects at +10 days after maximum it is predicted that there will be virtually no contamination by IMEs.

Hence, this is a good time to measure $v_{\rm edge}$. The effect of blends as a function of time can be seen in Figures 1–3. For subluminous SNe Ia, these blends mimic a rapid drop in the evolution of $v_{\rm edge}$ before +10 days as can be seen in the velocity evolution of SN 1999by (see Figure 3). For transitional SNe Ia, such as SN 2011iv, SNhunt281, and iPTF13ebh, the observed rapid drop in $v_{\rm edge}$ as a function of time can be understood as follows: $v_{\rm edge}$ is larger and is thus at lower densities compared to subluminous supernovae. These densities are close to the critical density ($\leqslant 10^{7\cdots 8}$ particles cm^{-3}), which marks the transition from allowed to forbidden lines. This results in a rapid drop of $v_{\rm edge}$. We note that, in normal-bright SNe, the temperatures are higher resulting is larger collisional rates, which depopulate the levels responsible for forbidden lines and delay the rapid drop in $v_{\rm edge}$.

In this work, we use the s_{BV} parameter defined in Burns et al. (2014) and used in Ashall et al. (2019), as well as $\Delta m_{15,s}(B)$ and $\Delta m_{15,s}(V)$. $\Delta m_{15,s}(B)$ and $\Delta m_{15,s}(V)$ (Höflich et al. 2010; Hoeflich et al. 2017), are modified decline rate parameters produced for a time base of $t = 15\,d * s$, with s being the stretch parameter of the LC as defined in Goldhaber et al. (2001). They can be parameterized by $\Delta m_{15,s}(B) = \frac{\Delta m_{(15\times s)}}{s}$. Normal SNe Ia have an $\Delta m_{15,s}(B)$ and $\Delta m_{15,s}(V)$ of $\sim$1.2 mag and 0.7 mag, respectively. We chose to use $\Delta m_{15,s}(B)$ and $\Delta m_{15,s}(V)$ as they can be theoretically interpreted as a measurement of diffusion timescales (Hoeflich et al. 2017), whereas the theoretical interpretation of s or s_{BV} is not straight forward but a combination of effects.

3. Brief Description of the Explosion Scenarios and Their Relation to LC Parameters

Normal, transitional, and subluminous SNe Ia can be thought to be in three different regimes. In the case of normal

[16] We note that Blondin et al. (2018) use incomplete nuclear reaction networks, and complete networks predict a larger ^{56}Ni production (Shen et al. 2018b). However, the velocity where $X_{\rm Ni} \approx 0.10$ in the complete networks is consistent with that of Blondin et al. (2018) within 500 km s^{-1}.

[17] We note that as these IME lines are very sensitive to the ionization state, whether epochs earlier than +10 days can be used to measure $v_{\rm edge}$ can be decided by the spectra of each specific SN.

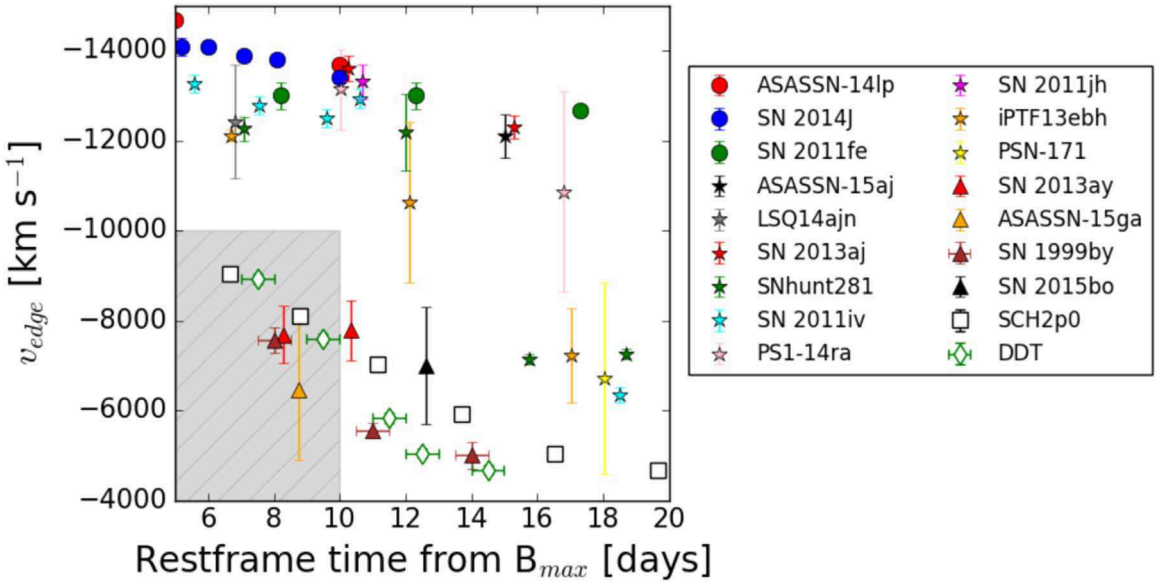

Figure 3. $v_{\rm edge}$ as a function of time from Ashall et al. (2019). For comparison, the $M_{\rm Ch}$ (open green diamonds) and sub-$M_{\rm Ch}$ (open black squares) models of the subluminous SN 1999by from Hoeflich et al. (2002) and Blondin et al. (2018) have been plotted. The gray shaded region is the area where the spectra may be affected by line blends and may not be suitable to be used for measuring the ^{56}Ni abundance, see Section 2 for details. For the subluminous SNe Ia, in the epochs where the measurement of $v_{\rm edge}$ is reliable, it is apparent that the sub-$M_{\rm Ch}$ model has values larger than the observations. Whereas the $M_{\rm Ch}$ models are in agreement with the observations. Normal SNe Ia are marked by solid circle symbols, transitional SNe Ia are marked by star circle symbols, and subluminous SNe Ia are marked by solid triangle symbols.

SNe Ia the opacity of the ejecta is dominated by doubly ionized species throughout most of the envelope, leading to a slowly declining post-maximum LC. Transitional SNe Ia are located in the area of rapidly decreasing luminosity in the LWR (Hoeflich et al. 2002, 2017; Ashall et al. 2018). This is the region where an SN Ia enters the regime of a quickly decreasing opacity in the envelope soon after maximum, due to an earlier onset of the recombination front that results in a faster release of stored energy. Whereas, subluminous SNe Ia are dominated by singly ionized species, which leads to a fast declining post-maximum LC.

Within spherical DDT models, for the brightest SNe Ia most of the ^{56}Ni is made in the detonation phase. Furthermore, in these models the ^{56}Ni production is an almost smooth function of $\rho_{\rm tr}$, but its relative change is quick between models. This is reflected by a rapidly decreasing luminosity over the transitional regime, which, to first order, is $\propto M(^{56}{\rm Ni})$. In other words, the ^{56}Ni production during the detonation phase changes from $\sim$0.3 to 0 $M_{\odot}$, as $\rho_{\rm tr}$ decreases from $\sim 1.8 \times 10^7$ g cm^{-3} to 0.8×10^7 g cm^{-3} over the transitional regime toward subluminous SNe Ia. For subluminous SNe Ia almost all of the ^{56}Ni is produced during the deflagration burning phase, which happens over an $\sim 0.25\,M_{\odot}$ range. This leads to a close to constant luminosity for subluminous SNe Ia and a ^{56}Ni production of 0.1–0.2 $M_{\odot}$ (e.g., Stritzinger et al. 2006), which is dependent on the rate of electron capture (Hoeflich et al. 2017; Gall et al. 2018).

In the sub-$M_{\rm Ch}$ models considered here a central explosion is triggered in a static WD (Blondin et al. 2018). These types of models are used as a proxy for a helium detonation, as well as the dynamically driven double-degenerate double-detonation scenario (Shen et al. 2018a). In these classes of models the mass of the WD is correlated to the luminosity and the light-curve shape. Lower mass WDs produce less effective burning, less nuclear statistical equilibrium (NSE) elements, less ^{56}Ni, less heating, lower opacities, and a faster LC.

4. The Relation of $v_{\rm edge}$ and LC Parameters

4.1. v_{edge} versus $s_{\rm BV}$

Here, we discuss $v_{\rm edge}$ as a function of light-curve color-stretch parameter, s_{BV}. As shown in Ashall et al. (2019) and as illustrated in the upper left panel of Figure 4, SNe with a larger s_{BV} are found to exhibit higher values of $v_{\rm edge}$.

A measure of $v_{\rm edge}$ serves as a powerful diagnostic tool because it is robust due to Doppler shifts that are well measured by spectra at the onset of the emergence of the *H*-band feature. For a comparison between data and theory, in Figure 4 we plot results obtained from non-LTE, spherical $M_{\rm Ch}$ DDT models (Hoeflich et al. 2017), as the open green diamonds. Note that in this figure the values of $v_{\rm edge}$ are obtained from four different DDT models (Model 23, 20, 12, and 8) of Hoeflich et al. (2017), whereas in Figure 3, one subluminous DDT model and one subluminous sub-$M_{\rm Ch}$ model are plotted as a function of time.

A comparison with the abundance structures of the DDT models shows that $v_{\rm edge}$ measures the point in velocity space where $X_{\rm Ni}$ falls to the order of 0.02–0.03, for the entire range from normal-bright to subluminous SNe Ia.

For burning to NSE, the density must be larger than $\approx 2 \times 10^7$ g cm^{-3}. In the DDT scenario, for normal-bright SNe Ia, $v_{\rm edge}$ corresponds to a region where the 2%–3% of ^{56}Ni required to form the emission feature is located between $\approx -13{,}000$ and $-10{,}000$ km s^{-1}. Because there is little mass involved in these layers, the change in the total amount of ^{56}Ni produced over this $v_{\rm edge}$ range is small and, consequently, the luminosity difference between normal SNe Ia is little.

There is a fast drop in $v_{\rm edge}$ over an s_{BV} range of $\sim$0.6–0.45, the mean $v_{\rm edge}$ drops from $\sim -11{,}500$ to ~ -5500 km s^{-1}. This is because the change in mass per unit velocity rapidly decreases with increasing velocity. From DDT models, the bright-transitional SNe Ia are characterized by an NSE production that is dominated by detonation burning, whereas

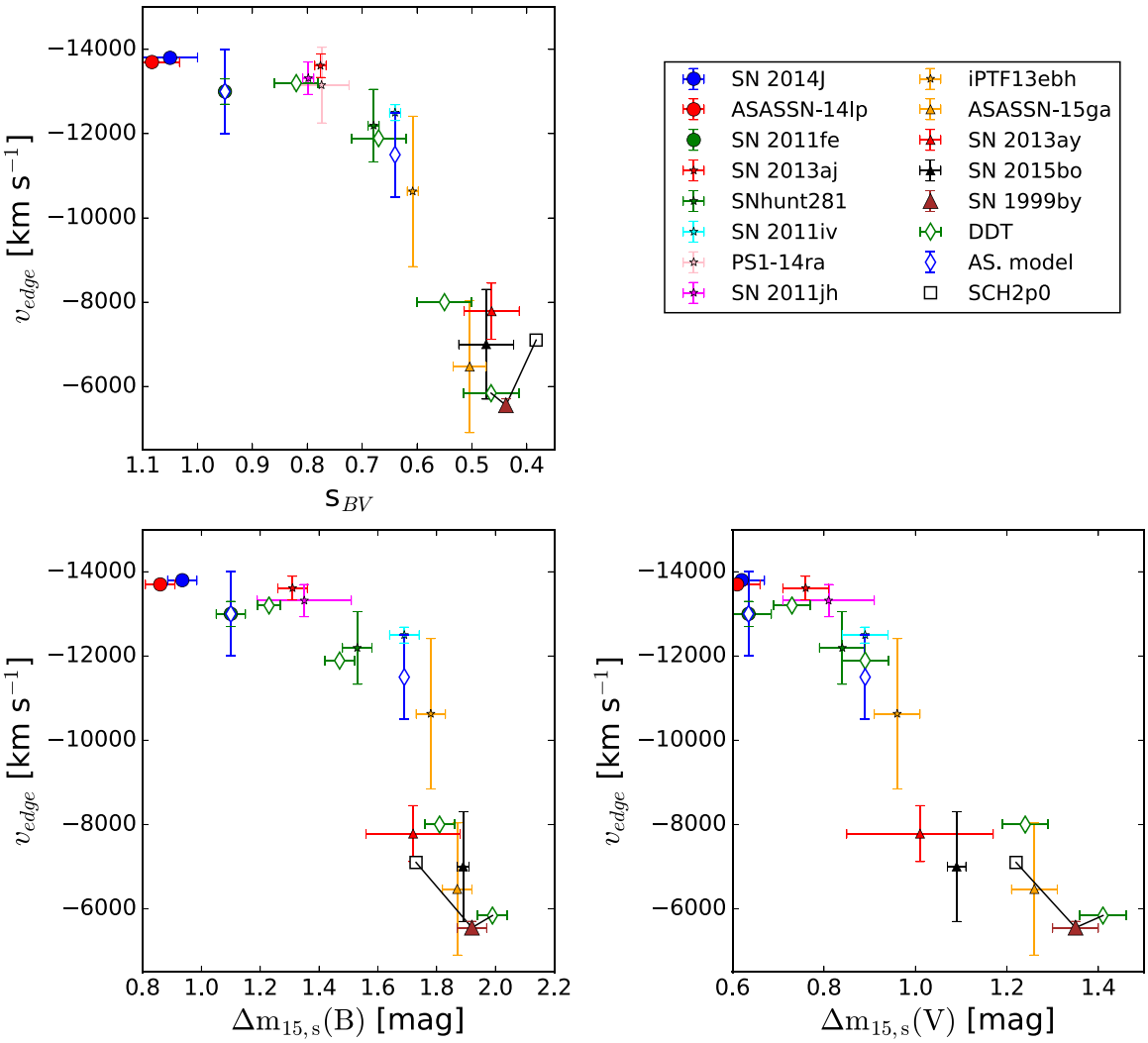

Figure 4. Upper left: the iron-peak outer velocity at $+10 \pm 3$ days as a function of s_{BV}, the open symbols are models and filled in symbols are observations. The open green diamonds are non-LTE $M_{\rm Ch}$ DDT models from Hoeflich et al. (2017), the open blue diamonds are the results from abundance stratification models for SN 2011fe and SN 2011iv from Mazzali et al. (2014) and Ashall et al. (2018), respectively, and the open black square is the SCH2p0 ($0.9 M_{\odot}$) model from Blondin et al. (2018). The solid black lines link SN 1999by with its sub-$M_{\rm Ch}$ and $M_{\rm Ch}$ models. These models therefore have the same luminosity as SN 1999by. Lower left: the same as the top left panel but as a function of $\Delta m_{15,s}(B)$. Lower right: the same as the top left panel but as a function of $\Delta m_{15,s}(V)$. In all panels the $M_{\rm Ch}$ models follow the observations, but the sub-$M_{\rm Ch}$ model has a velocity that is $\sim$1500 km s^{-1} larger than SN 1999by. Whereas the $M_{\rm Ch}$ model follows the observations. Normal SNe Ia are marked by solid circle symbols, transitional SNe Ia are marked by star circle symbols, and subluminous SNe Ia are marked by solid triangle symbols.

the less luminous transitional supernovae are dominated by deflagration burning. Because the densities are still low, a large relative change in the total NSE mass coincides with a large shift in $v_{\rm edge}$. Therefore, for transitional SNe Ia a uniform change in $\rho_{\rm tr}$ produces a significant drop in $v_{\rm edge}$. This drop in $v_{\rm edge}$ happens in the same regime as the luminosity drop in the LWR. However, these processes are not causally linked. Hence, $v_{\rm edge}$ is a complementary measurement of the SNe Ia physics and scenario, and it is not a proxy for the light-curve shape. This is because the diffusion timescales depend on the ^{56}Ni distribution, ^{56}Ni mass, and ejecta mass, whereas, $v_{\rm edge}$ only depends on the outer edge of the ^{56}Ni region, and measures the specific $E_{\rm kin}$. Finally, for subluminous SNe Ia, most of the NSE burning takes place during the deflagration phase in the inner, high-density regions, which produces a minimum value of $v_{\rm edge}$ at ~ -5500 km s^{-1}.

Two of the SN (SN 2011fe and SN 2011iv) in our work have been analyzed using the abundance stratification technique (Mazzali et al. 2014; Ashall et al. 2018). This method reverse engineers the abundance structure in the ejecta, using a comparison between observed and synthetic spectra (e.g., Stehle et al. 2005; Ashall et al. 2014, 2016b). We also plot the velocity of ^{56}Ni at 3% in abundance from these models (see the blue open diamonds in Figure 4). There is a good agreement, within $\sim$1000 km s^{-1} with the abundance stratification results, non-LTE DDT models, and observations. It should be noted that by definition the abundance stratification models have the same luminosity as their corresponding SNe.

4.2. SN 1999by

One supernova from the sample, SN 1999by a subluminous SN, has been modeled by both $M_{\rm Ch}$ (Hoeflich et al. 2002) and sub-$M_{\rm Ch}$ (Blondin et al. 2018) explosions, which makes it a perfect test case for this work. Therefore, included in Figure 4 is the sub-$M_{\rm Ch}$ model (SCH2p0) for the subluminous SN 1999by from Blondin et al. (2018; open black square). The SCH2p0 ($M_{\rm WD} = 0.9 M_{\odot}$) sub-$M_{\rm Ch}$ model has a velocity of -7000 km s^{-1}, which is much larger, by 1500 km s^{-1}, than

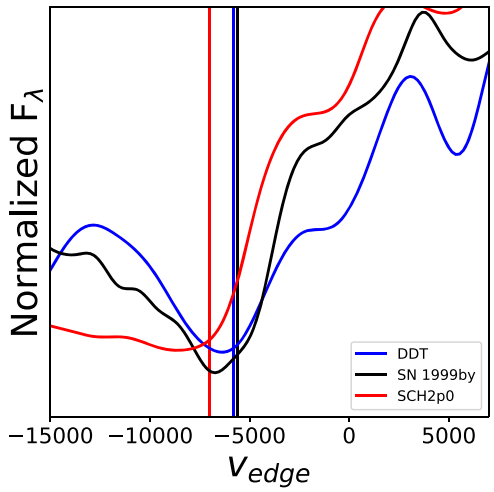

Figure 5. Comparison of the spectra of SN 1999by (black) at +11 days and models of M_{Ch} DDT explosion from Hoeflich et al. (2002; blue) and sub-M_{Ch} SCH2p0 explosion from Blondin et al. (2018; red). The spectra have been Gaussian smoothed with a sigma of 3. The vertical solid lines are located at the measured velocity of the minima. The velocity of the sub-M_{Ch} model ($v_{edge} = -7000 \pm 200$ km s^{-1}) is larger than both the observations ($v_{edge} = -5500 \pm 200$ km s^{-1}) and the M_{Ch} DDT model ($v_{edge} = -5800 \pm 200$ km s^{-1}). We note that vedge is not at the exact minimum of the feature because a continuum is subtracted in the fitting procedure, see Ashall et al. (2019). This makes the value of v_{edge} in the sub-Ch model closer to observations than the plot shows.

the observations. In this model v_{edge} corresponds to the region where the X_{Ni} is 0.10. This is due to a combination of geometric dilution and the lower mass meaning that a larger mass fraction is required to form the emission feature.

Figure 5 presents the spectra of SN 1999by (black) as well as the M_{Ch} DDT model (blue) from Hoeflich et al. (2002), and the sub-M_{Ch} model, SCH2p0, (red), from Blondin et al. (2018), all of which are at ∼+11 days relative to B-band maximum. Note that the models from Hoeflich et al. (2002) and Blondin et al. (2018) have similar B-band rise times of 14.5 days and 14.6 days, respectively. It is clear that the M_{Ch} DDT model produces the correct velocity compared to the observations, whereas the sub-M_{Ch} model has a value of v_{edge} which is too large.

As shown by both the M_{Ch} and sub-M_{Ch} models, v_{edge} is determined by the interplay between the mass of ^{56}Ni and the mass of IME formed in the explosion, because there is a steep drop in the abundances during the transition between NSE and incomplete Si-burning. This makes v_{edge} a stable measurement regardless of the explosion scenario. In effect, v_{edge} is a measure of the specific kinetic energy, E_{kin} ($M(^{56}\mathrm{Ni})/M_{WD}$), of the region. For a given $M(^{56}\mathrm{Ni})$, models with lower values of M_{WD} will result in systematically higher values of v_{edge}.

4.3. v_{edge} and $\Delta m_{15,s}(B)$, $\Delta m_{15,s}(V)$

s_{BV} measures the timing of the turnover in the color curves of SNe Ia, but as we will see below, may mask diversity. Therefore, we use the LC parameters $\Delta m_{15,s}(B)$ and $\Delta m_{15,s}(V)$ to analyze the correlation. The bottom panels in Figure 4 present v_{edge} as a function of $\Delta m_{15,s}(B)$ and $\Delta m_{15,s}(V)$. Once again the DDT models fit the data well, whereas the sub-M_{Ch} model is not close to SN 1999by.

Nine out of 10 SNe Ia in the plot are consistent with M_{Ch} DDT models. However, SN 2015bo, which has a high-cadence LC, with pre-maximum coverage, and will be the subject of a future individual analysis, has a large $\Delta m_{15,s}(B) = 1.89$ mag but a small $\Delta m_{15,s}(V) = 1.09$ mag. The combined values of LC shape and v_{edge} for SN 2015bo are inconsistent with both the DDT and sub-M_{Ch} models. For a $v_{edge} = -7000$ km s^{-1} DDT models predict a $\Delta m_{15,s}(B) = \sim 1.85$ mag and $\Delta m_{15,s}(V) = \sim 1.32$ mag, and sub-M_{Ch} models predict $\Delta m_{15,s}(B) = \sim 1.73$ mag and $\Delta m_{15,s}(V) = \sim 1.22$ mag. It is difficult to reconcile this deviation from the data and models by varying the physics of sub-M_{Ch} or M_{Ch} DDT explosions.

Dynamical merger models are characterized by red colors at maximum light, a slowly evolving V-band LC, a fast declining B-band LC, and have ^{56}Ni located at low velocities (Hoeflich & Khokhlov 1996; García-Berro & Lorén-Aguilar 2017). These properties make dynamical mergers a viable scenario for SN 2015bo, and demonstrate that there may be different explosion mechanisms and progenitor scenarios present within the subluminous SNe Ia population.

We note that, on its own, v_{edge} may not be able to distinguish between different models. The method here also requires accurate high-cadence LCs. For example, in the case of SN 2013ay where the photometric coverage begins at ∼+10 days, we cannot rule out either the sub-M_{Ch} or M_{Ch} mass models, despite having high signal-to-noise NIR spectra.

The diversity among SNe Ia is apparent when we combine $\Delta m_{15,s}$ and v_{edge}, and extra information may be obtained if the absolute luminosity ($M_{V,B}$) of the supernova is also utilized. Therefore, for further insights, we suggest that all three parameters are used. In the one supernova, SN 1999by, where we can accurately determine the absolute magnitude from observations, it is clear that the M_{Ch} model is favored. Combining absolute magnitude, with v_{edge} and light-curve shape will allow for future work to more accurately discriminate between explosion scenarios and models. For example, a transitional M_{Ch} explosion might have the same value of v_{edge} as a subluminous sub-M_{Ch} explosion, and both objects may have similar light-curve shapes, but different ^{56}Ni masses and absolute magnitudes. Therefore, combining all parameters will provide additional information.

5. Conclusion

Using the correlation found between light-curve shape and v_{edge} in Ashall et al. (2019), we have demonstrated that v_{edge} is a new comprehensive way to measure the outer edge of the ^{56}Ni region in SNe Ia ejecta. Brighter SNe Ia have ^{56}Ni located at higher velocities than subluminous SNe Ia (see Figure 4). This is consistent with previous results obtained by nebular phase spectral modeling (Mazzali et al. 1998; Botyánszki & Kasen 2017). Using SN 1999by as an example, we have also demonstrated that a combination of v_{edge}, $\Delta m_{15,s}$, and absolute magnitude can be a new method to probe for diversity and explosion scenarios in SNe Ia.

v_{edge} is a stable measurement that is determined by the interplay between the mass of ^{56}Ni and the mass of IME formed in the explosion, and corresponds to the sharp transition in the ejecta between complete and incomplete Si-burning regions.

v_{edge} measures the point in velocity space where X_{Ni} falls to the order of 0.03–0.10, and is dependent on the ejecta mass of the explosion. v_{edge} is stable when compared to models because it measures a Doppler shift that is dependent on the underlying abundance structure. v_{edge} only depends on the presence of Fe II and Co II at the edge of the ^{56}Ni region rather than the correct

absolute flux in the model. Furthermore, $v_{\rm edge}$ is an important tool for studying SNe Ia physics as it is independent of distance.

For subluminous SNe Ia, at early times, the edge of the *H*-band break may be contaminated by Ca II, Ca I, Si I, and S I lines. Therefore, we urge that caution should be used when choosing an epoch to measure $v_{\rm edge}$, because these line blends may artificially increase its value. The supernova needs to be in the ^{56}Ni-rich region, and not affected by line blends before measuring $v_{\rm edge}$. For the least luminous SNe Ia, this occurs around +10 days. Although, this value can be sensitive to the amount of mixing of ^{56}Ni in the explosion, and each time series of spectra should be examined on a case-by-case basis.

Within the framework of DDT models, the quick drop in the $v_{\rm edge}$ versus s_{BV} correlation for transitional SNe Ia is due to the rapidly changing expansion velocity as a function of mass. We demonstrated that $M_{\rm Ch}$ models may be able to reproduce the evolution of $v_{\rm edge}$ over the entire luminosity range of SNe Ia. However, the value of $v_{\rm edge}$ obtained from the sub-$M_{\rm Ch}$ model of the subluminous SN 1999by differs from the observations by $\sim$1500 km s^{-1}. This strongly favors high-mass explosions for the very subluminous SNe Ia. However, we cannot conclude that all of the subluminous SNe are inconsistent with sub-$M_{\rm Ch}$ models. It is possible that future sub-$M_{\rm Ch}$ models will overcome their current problems.

Additional distance-independent information can be obtained using $\Delta m_{15,s}(B)$ and $\Delta m_{15,s}(V)$ in combination with $v_{\rm edge}$. This allows for the diversity among low-luminosity SNe Ia to be probed. We find that SN 2015bo is inconsistent with both the spherical $M_{\rm Ch}$ DDT models and sub-$M_{\rm Ch}$ models considered here, but may have characteristics of a dynamical merger model, which adds to the evidence for diversity among the subluminous population.

One of the limitations of our study includes the fact that we have only used published non-LTE models with NIR spectra. However, in the future, the method presented here should be applied to a diverse set of explosion scenarios and models, as well as observations of SNe Ia which belong to different areas of the luminosity–width relation.

Our analysis here favors high $M_{\rm WD}$ explosions for all of the supernovae examined. However, it appears that there could be multiple explosion mechanisms among subluminous SNe Ia, and NIR spectra can reveal this diversity. We are beginning to obtain a full view of the SNe Ia phenomenon ranging from early time studies (e.g., Hosseinzadeh et al. 2017; Stritzinger et al. 2018), to mid-infrared studies (e.g., Telesco et al. 2015; Hoeflich et al. 2018), and NIR studies (e.g., Hsiao et al. 2019; Ashall et al. 2019). Simultaneously examining all of these phenomena and comparing them to modern explosion models may let us unlock the mysteries about what SNe Ia are, which will enable us to improve upon the utility of these objects as distance indicators. Looking toward the future, we believe that $v_{\rm edge}$ will help us understand the physical nature of the SNe Ia and how they explode.

In memory of Alexei Khokhlov, a great scientist and friend from whom we learned so much over the years. We want to thank many colleagues for helpful discussions. This work has been supported in part by NSF awards AST-1008343 and AST-1613426 (PI: M.M. Phillips), AST-1613472 (PI: E.Y.H.), AST-1715133 (PI: P.H.), AST-1613455 (PI:N.S.), and in part by a Sapere Aude Level II grant (PI: M.D.S. provided by the Danish National Research Foundation (DFF). M.D.S. is funded by a research grant (13261) from the VILLUM FONDEN. E.B. acknowledges partial support from NASA grant NNX16AB25G. E.B. and M.D.S. thank the Aarhus University Research Fund (AUFF) for a Sabbatical research grant. Research by D.J.S. is supported by NSF grants AST-1821967, 1821987, 1813708, and 1813466. N.B.S. and K.K. also thank George P. and Cynthia Woods Mitchell Institute for Fundamental Physics and Astronomy for support during this research.

Appendix

In Figure 6 we present the $v_{\rm edge}$ fits of the $M_{\rm Ch}$, sub-$M_{\rm Ch}$ and data of SN 1999by, the fitting procedure from Ashall et al. (2019) was followed. The small differences between the minima of the fits and the data/models are on the order of 200 km s^{-1}, which is well with the error bars, and therefore does not affect the conclusions above.

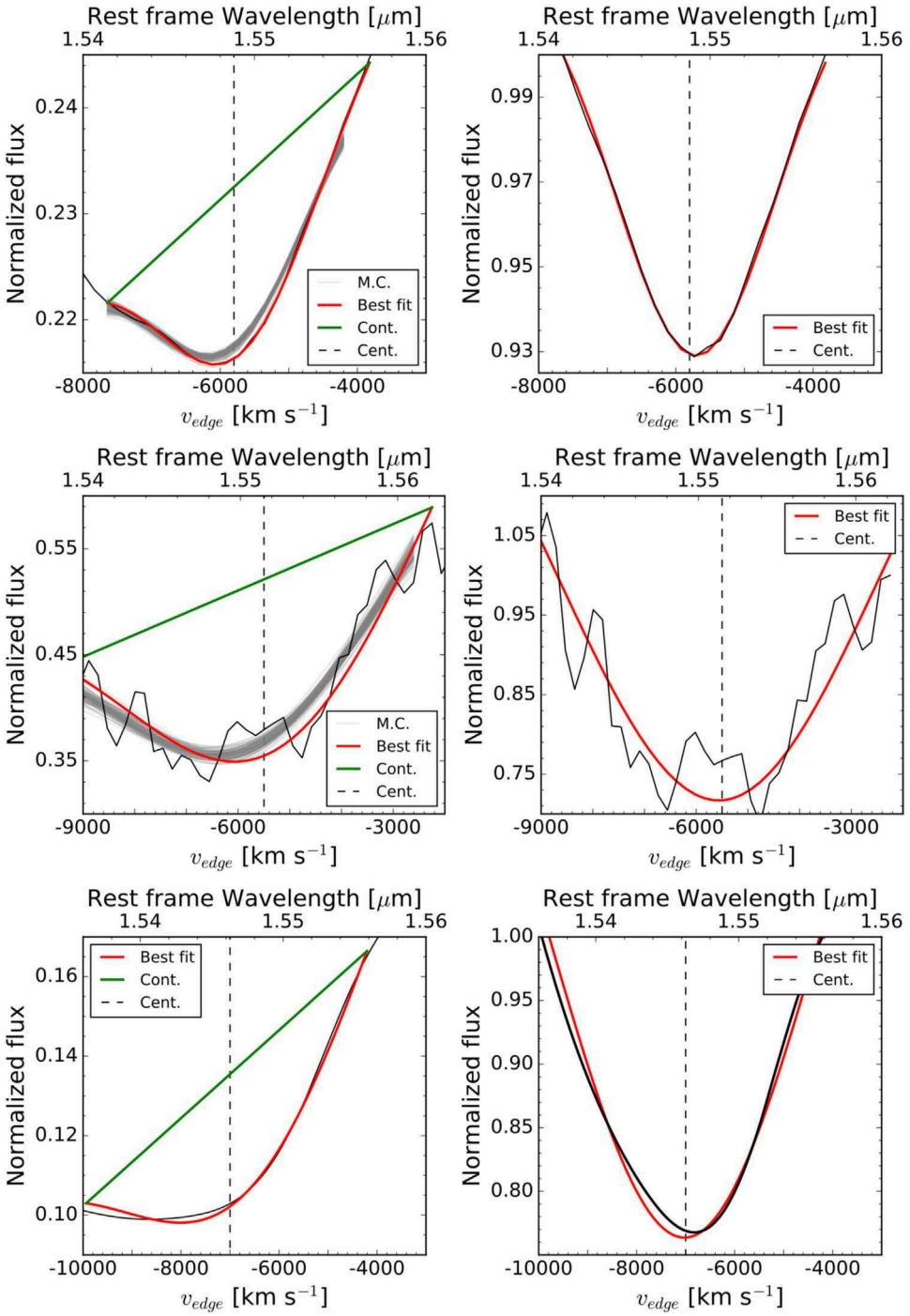

Figure 6. The $v_{\rm edge}$ fits of the subluminous $M_{\rm Ch}$ model (top panels), SN 1999by (middle panels), and the subluminous sub-$M_{\rm Ch}$ model (bottom panels). The black lines are the data or models, the red lines denote the best fits, the light gray lines correspond to the MC fits, the green lines are continua that were subtracted, and the vertical dashed line indicates the minima of the best fit and the value of $v_{\rm edge}$.

ORCID iDs

C. Ashall https://orcid.org/0000-0002-5221-7557
P. Hoeflich https://orcid.org/0000-0002-4338-6586
M. M. Phillips https://orcid.org/0000-0003-2734-0796
M. Stritzinger https://orcid.org/0000-0002-5571-1833
E. Baron https://orcid.org/0000-0001-5393-1608
A. L. Piro https://orcid.org/0000-0001-6806-0673
K. Krisciunas https://orcid.org/0000-0002-6650-694X
N. Morrell https://orcid.org/0000-0003-2535-3091
D. J. Sand https://orcid.org/0000-0003-4102-380X

References

Arnett, W. D. 1982, ApJ, 253, 785
Ashall, C., Hsiao, E. Y., Hoeflich, P., et al. 2019, ApJL, 875, 14
Ashall, C., Mazzali, P., Bersier, D., et al. 2014, MNRAS, 445, 4427
Ashall, C., Mazzali, P., Sasdelli, M., & Prentice, S. J. 2016a, MNRAS, 460, 3529
Ashall, C., Mazzali, P. A., Pian, E., & James, P. A. 2016b, MNRAS, 463, 1891
Ashall, C., Mazzali, P. A., Stritzinger, M. D., et al. 2018, MNRAS, 477 153
Blondin, S., Dessart, L., & Hillier, D. J. 2015, MNRAS, 448, 2766
Blondin, S., Dessart, L., & Hillier, D. J. 2018, MNRAS, 474, 3931

Blondin, S., Dessart, L., Hillier, D. J., & Khokhlov, A. M. 2017, MNRAS, 470, 157
Blondin, S., Kasen, D., Röpke, F. K., Kirshner, R. P., & Mandel, K. S. 2011, MNRAS, 417, 1280
Botyánszki, J., & Kasen, D. 2017, ApJ, 845, 176
Bulla, M., Sim, S. A., Kromer, M., et al. 2016a, MNRAS, 462, 1039
Bulla, M., Sim, S. A., Pakmor, R., et al. 2016b, MNRAS, 455, 1060
Burns, C. R., Stritzinger, M., Phillips, M. M., et al. 2014, ApJ, 789, 32
Childress, M. J., Hillier, D. J., Seitenzahl, I., et al. 2015, MNRAS, 454, 3816
Dan, M., Guillochon, J., Brüggen, M., Ramirez-Ruiz, E., & Rosswog, S. 2015, MNRAS, 454, 4411
Dan, M., Rosswog, S., Brüggen, M., & Podsiadlowski, P. 2014, MNRAS, 438, 14
Dhawan, S., Flörs, A., Leibundgut, B., et al. 2018, A&A, 619, A102
Dhawan, S., Leibundgut, B., Spyromilio, J., & Blondin, S. 2017, A&A, 602, A118
Diamond, T. R., Hoeflich, P., Hsiao, E. Y., et al. 2018, ApJ, 861, 119
Fesen, R. A., Höflich, P. A., Hamilton, A. J. S., et al. 2007, ApJ, 658, 396
Filippenko, A. V., Richmond, M. W., Branch, D., et al. 1992, AJ, 104, 1543
Fink, M., Hillebrandt, W., & Röpke, F. K. 2007, A&A, 476, 1133
Gall, C., Stritzinger, M. D., Ashall, C., et al. 2018, A&A, 611, A58
Gamezo, V. N., Khokhlov, A. M., & Oran, E. S. 2005, ApJ, 623, 337
García-Berro, E., & Lorén-Aguilar, P. 2017, in Handbook of Supernovae, ed. A. W. Alsabti & P. Murdin (Berlin: Springer), 1237
Goldhaber, G., Groom, D. E., Kim, A., et al. 2001, ApJ, 558, 359
Goldstein, D. A., & Kasen, D. 2018, ApJL, 852, L33
Hoeflich, P., Ashall, C., Fisher, A., et al. 2018, arXiv:1810.05910
Hoeflich, P., Gerardy, C. L., Fesen, R. A., & Sakai, S. 2002, ApJ, 568, 791
Hoeflich, P., Hsiao, E. Y., Ashall, C., et al. 2017, ApJ, 846, 58
Hoeflich, P., & Khokhlov, A. 1996, ApJ, 457, 500
Höflich, P., Krisciunas, K., Khokhlov, A. M., et al. 2010, ApJ, 710, 444
Hosseinzadeh, G., Sand, D. J., Valenti, S., et al. 2017, ApJL, 845, L11
Hristov, B., Collins, D. C., Hoeflich, P., Weatherford, C. A., & Diamond, T. R. 2018, ApJ, 858, 13
Hsiao, E. Y., Burns, C. R., Contreras, C., et al. 2015, A&A, 578, A9
Hsiao, E. Y., Marion, G. H., Phillips, M. M., et al. 2013, ApJ, 766, 72
Hsiao, E. Y., Philips, M. M., Marion, G. H., et al. 2019, PASP, 131, 014002
Hsiao, Y. C. E. 2009, PhD thesis, Univ. Victoria
Jordan, G. C., IV, Fisher, R. T., Townsley, D. M., et al. 2008, ApJ, 681, 1448
Kasen, D., Röpke, F. K., & Woosley, S. E. 2009, Natur, 460, 869
Khokhlov, A. M. 1991, A&A, 245, 114
Leibundgut, B., Kirshner, R. P., Phillips, M. M., et al. 1993, AJ, 105, 301
Livne, E. 1990, ApJL, 354, L53
Livne, E., & Arnett, D. 1995, ApJ, 452, 62
Maeda, K., Benetti, S., Stritzinger, M., et al. 2010, Natur, 466, 82
Mazzali, P. A., Cappellaro, E., Danziger, I. J., Turatto, M., & Benetti, S. 1998, ApJL, 499, L49
Mazzali, P. A., Röpke, F. K., Benetti, S., & Hillebrandt, W. 2007, Sci, 315, 825
Mazzali, P. A., Sullivan, M., Hachinger, S., et al. 2014, MNRAS, 439, 1959
Nomoto, K., Iwamoto, K., Nakasato, N., et al. 1997, NuPhA, 621, 467
Nugent, P., Baron, E., Branch, D., Fisher, A., & Hauschildt, P. H. 1997, ApJ, 485, 812
Pakmor, R., Kromer, M., Taubenberger, S., et al. 2012, ApJL, 747, L10
Patat, F., Höflich, P., Baade, D., et al. 2012, A&A, 545, A7
Phillips, M. M. 1993, ApJL, 413, L105
Phillips, M. M., Contreras, C., Hsiao, E. Y., et al. 2019, PASP, 131, 014001
Phillips, M. M., Lira, P., Suntzeff, N. B., et al. 1999, AJ, 118, 1766
Piersanti, L., Gagliardi, S., Iben, I., Jr., & Tornambé, A. 2003, ApJ, 598, 1229
Polin, A., Nugent, P., & Kasen, D. 2018, arXiv:1811.07127
Poludnenko, A. Y., Gardiner, T. A., & Oran, E. S. 2011, PhRvL, 107 054501
Röpke, F. K., Hillebrandt, W., Schmidt, W., et al. 2007, ApJ, 668, 1132
Scalzo, R. A., Parent, E., Burns, C., et al. 2019, MNRAS, 483, 628
Scalzo, R. A., Ruiter, A. J., & Sim, S. A. 2014, MNRAS, 445, 2535
Shen, K. J., Boubert, D., Gänsicke, B. T., et al. 2018a, ApJ, 865, 15
Shen, K. J., Kasen, D., Miles, B. J., & Townsley, D. M. 2018b, ApJ, 854, 52
Shen, K. J., & Moore, K. 2014, ApJ, 797, 46
Sim, S. A., Röpke, F. K., Hillebrandt, W., et al. 2010, ApJL, 714, L52
Stehle, M., Mazzali, P. A., Benetti, S., & Hillebrandt, W. 2005, MNRAS, 360, 1231
Stritzinger, M., Mazzali, P. A., Sollerman, J., & Benetti, S. 2006, A&A, 460, 793
Stritzinger, M. D., Shappee, B. J., Piro, A. L., et al. 2018, ApJL, 864, L35
Tanaka, M., Mazzali, P. A., Stanishev, V., et al. 2011, MNRAS, 410, 1725
Telesco, C. M., Höflich, P., Li, D., et al. 2015, ApJ, 798, 93
Turatto, M., Benetti, S., Cappellaro, E., et al. 1996, MNRAS, 283, 1
Umeda, H., Nomoto, K., Kobayashi, C., Hachisu, I., & Kato, M. 1999, ApJL, 522, L43
Wheeler, J. C., Höflich, P., Harkness, R. P., & Spyromilio, J. 1998, ApJ, 496, 908
Whelan, J., & Iben, I., Jr. 1973, ApJ, 186, 1007
Woosley, S. E., & Weaver, T. A. 1994, ApJ, 423, 371
Yamaoka, H., Nomoto, K., Shigeyama, T., & Thielemann, F.-K. 1992, ApJL, 393, L55